The influence of high grain boundary density on helium retention in tungsten

G. Valles [a],[*], C. González [b], I. Martin-Bragado [c], R. Iglesias [b], J.M. Perlado [a], A. Rivera [a]

[a] *Instituto de Fusión Nuclear UPM, José Gutiérrez Abascal 2, 28006 Madrid, Spain*
[b] *Departamento de Física, Universidad de Oviedo, C/ Calvo Sotelo, s/n, Oviedo, Spain*
[c] *IMDEA Materials Institute, C/ Enric Kandel 2, 28906 Getafe, Madrid, Spain*

HIGHLIGHTS

- Comparison between monocrystalline and nanostructured irradiated tungsten.
- OKMC parameterization published and new DFT data.
- Important role of grain boundary density on defect evolution.
- Cluster pressurization much lower in nanostructured tungsten.
- Promising expectations on nanocrystalline tungsten in view of results.

ARTICLE INFO

ABSTRACT

In order to study the influence of a high grain boundary density on the amount, size and distribution of defects produced by pulsed helium (625 keV) irradiation in tungsten, we have carried out Object Kinetic Monte Carlo (OKMC) simulations in both monocrystalline and nanocrystalline tungsten. The parameterization of the OKMC code (MMonCa) includes binding energies obtained with our in-house Density Functional Theory (DFT) calculations. In the interior of a grain in nanocrystalline tungsten the mixed He_nV_m clusters are larger and have a lower He/V ratio. Thus, they are less pressurized clusters. The total elastic strain energy remains almost constant with the increasing number of pulses, contrary to its increase in monocrystalline tungsten. A better response to helium irradiation is therefore expected in nanocrystalline tungsten, opening a new path to investigate these nanostructured materials for fusion purposes.

© 2014 Elsevier B.V. All rights reserved.

1. Introduction

Tungsten has been proposed as a convenient material for plasma-facing components (PFC) in future fusion reactors since it offers several advantages: high melting point, high thermal conductivity, low sputtering coefficient and low tritium retention. Owing to these properties, tungsten is expected to be suitable for the first-wall and the divertor in magnetic fusion reactors and the first-wall (armour) in inertial fusion confinement chambers [1–4]. In both technologies the most adverse irradiation events are of pulsed nature: in the case of IFE (Inertial Fusion Energy) due to the target explosions in which the technology is based and in the case of MFE (Magnetic Fusion Energy) because of the edge-localized modes [5], which up to now (e.g., ITER) are intrinsic to TOKAMAK operation in H-mode.

In direct-target IFE, the energy will be released as follows: ∼1% in the form of X-rays with a pulse duration of a few ns, not considered to be a great threat to the wall; ∼71% due to pulsed neutron irradiation, of which energy will be absorbed beyond the first-wall; and ∼27% due to pulsed ion irradiation (burn products and debris ions) [6,7]. The resulting intense ion pulses will cause, on the one hand, very high thermal loads and on the other hand, damage due to Frenkel-Pair (FP) production and ion retention. Provided that the first wall is situated far enough from the target explosions, an acceptable thermo-mechanical response is feasible [8–10]. As regards the damage, different ions and burn products will reach the first wall, He ions among them [11]. The energy of He ions can be as high as 4 MeV with an average value of ∼2.5 MeV after thermalization in the compressed target [12], more than enough to produce Frenkel Pairs. Since He is not soluble in tungsten, He atoms tend to nucleate inside vacancies, which could result under certain circumstances in dramatic He bubble formation [13,14]. In general, He_nV_m clusters (not only large bubbles) cause microstructural changes [15,16], that may develop into blistering, cracking

and exfoliation of the material [17,18], all of them detrimental to the armour [19]. Experimental results show that continuous He irradiation (typical flux 10^{10}–10^{14} cm^{-2} s^{-1}) leads to deleterious effects (adverse porosity) at fluences higher than 10^{17}–10^{18} He cm^{-2} [15,17]. However, Renk et al. [6] showed that pulsed He irradiation (with fluxes up to 2×10^{19} cm^{-2} s^{-1}) leads to detrimental effects (pore formation and protrusions) at fluences as low as 10^{15} He cm^{-2}.

Many efforts are being carried out in order to mitigate the effect of He retention. A possible solution would be the use of nanostructured tungsten due to its large grain-boundary density: As grain boundaries may act as defect sinks for vacancies, interstitials and He atoms, nanostructured tungsten is expected to present higher irradiation tolerance [20]. The defects are supposed to accumulate at grain boundaries, where vacancies and self interstitial atoms (SIAs) annihilate [21]. On the other hand, He atoms can become trapped if the binding energy is high enough and diffusivity along the grain boundaries is low. Nanocolumnar tungsten has recently been fabricated with a high grain boundary density [22] and it has been experimentally observed that a high grain boundary density has a direct influence in the retention of light species [23]. A point not elucidated yet is whether inter-grain He migration allows for efficient He release or if the distribution and size of defects in the interior of a grain is affected by the high density of grain boundaries.

In the present study, we investigate the influence of high grain-boundary density in damage production by pulsed He irradiation in tungsten, by comparing monocrystalline tungsten (MW) to nanocrystalline tungsten (NW). We have carried out OKMC (Object Kinetic Monte Carlo) simulations parameterized with the aid of DFT calculations to describe the damage distribution in both materials. MMonCa code was used for this purpose [24,25]. In order to compare the influence of high grain-boundary density in the damage distribution in both nanocrystalline and monocrystalline tungsten, we have carried out two different sets of simulations with the experimental conditions used by Renk et al. in Ref. [6].

2. Simulation methods

2.1. Density Functional Theory (DFT) calculations

Calculations based on DFT techniques were performed using the *Vienna Ab initio Simulation Package* (VASP) [26–28]. The PBE [29] parameterization of the Generalized Gradient Approximation (GGA) for the exchange and correlation functional was used as well as the Plane Augmented Wave pseudopotentials [30], provided by the code. Six valence electrons have been considered for W (4 3d and 2 4s) and two 1s valence electrons for He. Within these approximations, the lattice parameter was estimated to be 3.172 Å, using an energy cutoff for the plane waves of 479 eV. The $5 \times 5 \times 5$ cubic supercell (250 W atoms) used in this work is built repeating the unit cell five times along each direction while 64 k-points sampled the first Brillouin zone. Several He atoms will be placed inside the unit cell in combination with n-vacancies (for n up to 4). Each structure is fully relaxed until the forces on all atoms are smaller than 0.025 eV/Å. The resulting final total energy is used to obtain the formation and binding energies for the subsequent OKMC simulations. The general equation giving the formation energy for a system formed by N_W and N_{He} atoms can be written as:

$$E_f = E_{tot} - N_W E(W) - N_{He} E(He) \tag{1}$$

where E_{tot} is the final total energy obtained in the relaxation of each supercell, $E(W)$ is the atomic energy of one metal atom inside the pure bulk when a $5 \times 5 \times 5$ supercell is used and $E(He)$ corresponds

to an isolated He atom located inside an otherwise empty $5 \times 5 \times 5$ box with sides equal to the equilibrium lattice parameter of the pure metal. On the other hand, the binding energy E_b corresponds to the energy released when two objects (in general more) merge to become a mixed one. It is defined as the formation energy difference between a system in which the objects are close together and a system in which the objects are far apart. Therefore, the formation energy of the configurations where the objects are separated is usually calculated individually in a supercell for each of the objects, as defined in Eq. (1). The general expression for E_b for a system with N_{def} defects (SIAs, n-vacancies and/or He atoms) can then be written as:

$$E_b(N_{def}) = \sum_{i_{def}=1}^{N_{def}} E_f(i_{def}) - E_f(N_{def}) \tag{2}$$

2.2. Object Kinetic Monte Carlo (OKMC)

OKMC simulations were carried out with our recently developed OKMC Open Source code MMonCa [24,25]. OKMC allows simulating large spatial regions (up to several μm³) on large timescales (from minutes to hours). As described in Ref. [24] He atoms, SIAs, vacancies and their clusters are considered as objects, which can migrate, dissociate from or agglomerate into clusters, desorb from free surfaces or annihilate in the case of vacancies (V) and self interstitial atoms (SIAs), often abbreviated simply as interstitials (I), i.e., V + I → Ø. Cluster agglomeration, desorption and annihilation events take place when two objects interact geometrically (an interaction radius is defined for each object). Migration and dissociation probabilities are calculated via an Arrhenius law:

$$v = v_0 \cdot e^{-\left(\frac{E^{event}}{k_B T}\right)} \tag{3}$$

where v_0 is the prefactor, k_B the Boltzmann constant, T the temperature and E^{event} is the corresponding activation barrier (migration or dissociation energy). The dissociation energy is the sum of the migration energy of the emitted object plus the binding energy of this object to the trapping cluster. Clusters can only emit single particles (a single vacancy, a SIA or a He atom in this work). The prefactor and the activation energy must be set for each migration or dissociation event.

We have parameterized object migration values in MMonCa following the scheme published by Becquart et al. [31,32]. The prefactors and migration energies for all mobile objects can be seen in Table 1. Mixed He$_n$V$_m$ and He$_n$I$_m$ clusters are considered immobile (with the exception of HeV, HeV$_2$ and HeV$_3$ [33]). Pure He cluster

Table 1
Prefactor and migration energy (eV) for mobile objects: He, single vacancy, SIA, pure He clusters, vacancy clusters and SIA clusters as published by Becquart et al. in Ref. [32]. The values of the constants are $v_0 = 6 \times 10^{12}$ s^{-1}, $q = 1000$ and $s = 0.5$. In the case of HeV$_m$ (only HeV, HeV$_2$ and HeV$_3$), migration energies have been calculated by us in Ref. [33]. We have considered their prefactors as v_0/m, in order to reproduce the movement of the whole cluster as the result of single jumps of the m-vacancies.

Object	Prefactor (s^{-1})	Migration energy (eV)
He	$10^{-2} v_0$	0.01
He$_2$	$10^{-2} v_0$	0.03
He$_3$	$10^{-2} v_0$	0.05
He$_n$, $n > 3$	$10^{-2} v_0$	$E_{mig}(He_{n-1}) + 0.01$
V	v_0	1.66
V$_m$, $m > 1$	$v_0 (q^{-1})^{m-1}$	1.66
I	v_0	0.013
I$_m$, $m > 1$	v_0 m^{-s}	0.013
HeV	v_0	4.83
HeV$_2$	$v_0/2$	2.04
HeV$_3$	$v_0/3$	1.94

Table 2
Binding energies obtained by DFT calculations for pure He, pure vacancy and pure SIA clusters published by Becquart et al. [31,32]. The binding energies for larger vacancy and SIA clusters are obtained by the capillary approximation, where $E_f(V) = 3.23$ eV and $E_f(I) = 9.96$ eV [32].

Cluster	Particle binding energy (eV)
$He + He \rightarrow He_2$	1.03
$He + He_2 \rightarrow He_3$	1.36
$He + He_3 \rightarrow He_4$	1.52
$He + He_4 \rightarrow He_5$	1.64
$He + He_5 \rightarrow He_6$	2.09
$He + He_6 \rightarrow He_7$	2.18
$He + He_7 \rightarrow He_8$	2.15
$He + He_8 \rightarrow He_9$	2.11
$V + V \rightarrow V_2$	−0.1
$V + V_2 \rightarrow V_3$	0.04
$V + V_3 \rightarrow V_4$	0.64
$V + V_4 \rightarrow V_5$	0.72
$V + V_5 \rightarrow V_6$	0.89
$V + V_6 \rightarrow V_7$	0.72
$V + V_7 \rightarrow V_8$	0.88
$V + V_{n-1}, n > 8 \rightarrow V_n$	$E_b(V_n) = E_f(V) + [E_b(V_2) - E_f(V)][n^{2/3} - (n-1)^{2/3}]/(2^{2/3} - 1)$
$I + I \rightarrow I_2$	2.12
$I + I_2 \rightarrow I_3$	3.02
$I + I_3 \rightarrow I_4$	3.6
$I + I_4 \rightarrow I_5$	3.98
$I + I_5 \rightarrow I_6$	4.27
$I + I_6 \rightarrow I_7$	5.39
$I + I_{n-1}, n > 8 \rightarrow I_n$	$E_b(I_n) = E_f(I) + [E_b(I_2) - E_f(I)][n^{2/3} - (n-1)^{2/3}]/(2^{2/3} - 1)$

mobility decreases as the number of He atoms being part of the cluster increases. Pure vacancy (V_m) and pure interstitial (I_m) clusters have constant migration energy (the migration energy of a single V and a single SIA respectively) and their migration prefactors follow decreasing laws, the larger the cluster the lower the migration prefactor (see Table 1).

In the case of the dissociation event, we considered a constant value for prefactors ($\nu_0 = 6 \times 10^{12}$ s^{-1}) of the order of the Debye frequency [32]. The binding energy for pure He, pure vacancy and pure SIA clusters [31,32] are summarized in Table 2.

The binding energy between He and SIAs is 0.94 eV [32]. With regard to the mixed He_nV_m clusters, the binding energies of one He atom to mixed He_nV_m clusters with up to 4 vacancies and 4 He atoms have been calculated with our DFT calculations. The

binding energies of single vacancy to mixed He_nV_m have been calculated from these values (see Table 3) and they are similar to those obtained by DFT calculations in Ref. [31]. Larger clusters are desirable, but the large number of He configurational positions inside the vacancy clusters makes these simulations very tedious and computationally demanding. In the case of one single vacancy, we calculated up to the 9th He atom (see Table 3) and it turned out that one additional He atom, i.e., the 10th He atom escapes from the vacancy region, defined as the free space in the complete $1 \times 1 \times 1$ unit cell. Due to this result, we consider a maximum of 9 He atoms per vacancy inside He_nV_m clusters, as pointed out in previous works [34,35]. In the molecular dynamics (MD) studies carried out by Henriksson et al. [36], the authors did not fix such a limit and, however, they observed that clusters with only 3 He atoms can promote the production of <1 1 1> crowdion interstitials. They explain this result by the influence of the nearby surface. In our case, the ion range in the 625 keV He implantations is ~1000 nm, too far away from the surface to consider that it plays a role on defect evolution. The parameterization was completed with data published by Becquart [31,32].
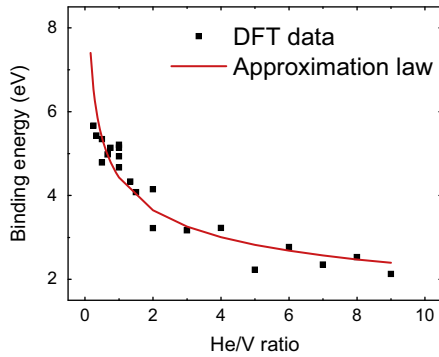
The binding energies of a He atom to He_nV_m clusters calculated by DFT are plotted as a function of the He/V ratio in Fig. 1. In addition, a potential law fit to the data (approximation function) is included. We have considered the binding energies given by the approximation function for clusters whose binding energy has not explicitly been calculated by DFT. Note that this approximation is in good agreement with DFT data at high He/V ratio but it does not provide a good approximation at very low He/V ratio, i.e., large vacancy clusters with few He atoms. In a recent paper [37], Juslin and Wirth propose a He binding energy of ~6 eV in clusters up to $He_{m-1}V_m$ ratio, close to the formation energy of an interstitial He (6.25 eV according to our DFT calculations). These values have been included in our parameterization.

In order to validate the parameterization for high temperatures, we have reproduced the experimental conditions published by Debelle et al. [38]. They implanted 60 keV He^3 ions at room temperature at a fluence of 2×10^{13} cm^{-2}. After the implantation, one sample was kept as reference and five other samples were annealed during one hour at different temperatures (1473 K, 1573 K, 1673 K, 1773 K and 1873 K). After the annealing processes, they measured the released He fraction with respect to that at the

Table 3
Binding energies of a He atom to a mixed He_nV_m cluster or to a pure V_m cluster calculated by DFT simulations as described in Section 2. One He atom binds strongly to pure V_m clusters. The more He atoms present in a defined He_nV_m cluster, the lower the binding energy of a new He atom. From these values we also calculated the binding energies of a vacancy to a mixed He_nV_m cluster o to a pure He_n cluster. The resulting values are similar to those published in Ref. [31].

Cluster	He binding energy (eV)	Cluster	V binding energy (eV)
$He + V \rightarrow HeV$	4.67	$V + He \rightarrow HeV$	4.67
$He + HeV \rightarrow He_2V$	3.22	$V + He_2 \rightarrow He_2V$	6.84
$He + He_2V \rightarrow He_3V$	3.17	$V + He_3 \rightarrow He_3V$	8.63
$He + He_3V \rightarrow He_4V$	3.23	$V + He_4 \rightarrow He_4V$	10.25
$He + He_4V \rightarrow He_5V$	2.23	$V + He_5 \rightarrow He_5V$	9.81
$He + He_5V \rightarrow He_6V$	2.77	$V + He_6 \rightarrow He_6V$	9.68
$He + He_6V \rightarrow He_7V$	2.35	$V + He_7 \rightarrow He_7V$	8.94
$He + He_7V \rightarrow He_8V$	2.53	$V + He_8 \rightarrow He_8V$	8.24
$He + He_8V \rightarrow He_9V$	2.13	$V + He_9 \rightarrow He_9V$	7.01
$He + V_2 \rightarrow HeV_2$	4.79	$V + HeV \rightarrow HeV_2$	−0.02
$He + HeV_2 \rightarrow He_2V_2$	4.93	$V + He_2V \rightarrow He_2V_2$	1.69
$He + He_2V_2 \rightarrow He_3V_2$	4.08	$V + He_3V \rightarrow He_3V_2$	2.6
$He + He_3V_2 \rightarrow He_4V_2$	4.15	$V + He_4V \rightarrow He_4V_2$	3.52
$He + V_3 \rightarrow HeV_3$	5.43	$V + HeV_2 \rightarrow HeV_3$	0.63
$He + HeV_3 \rightarrow He_2V_3$	4.98	$V + He_2V_2 \rightarrow He_2V_3$	0.68
$He + He_2V_3 \rightarrow He_3V_3$	5.14	$V + He_3V_2 \rightarrow He_3V_3$	1.74
$He + He_3V_3 \rightarrow He_4V_3$	4.33	$V + He_4V_2 \rightarrow He_4V_3$	1.92
$He + V_4 \rightarrow HeV_4$	5.67	$V + HeV_3 \rightarrow HeV_4$	0.83
$He + HeV_4 \rightarrow He_2V_4$	5.34	$V + He_2V_3 \rightarrow He_2V_4$	1.2
$He + He_2V_4 \rightarrow He_3V_4$	5.13	$V + He_3V_3 \rightarrow He_3V_4$	1.2
$He + He_3V_4 \rightarrow He_4V_4$	5.21	$V + He_4V_3 \rightarrow He_4V_4$	2.08

Fig. 1. Binding energy (eV) of a He atom to a mixed He_nV_m cluster, as a function of its He/V ratio. DFT data (black squares) have been approximated by a potential law (red line). (For interpretation of the references to color in this figure legend, the reader is referred to the web version of this article.)
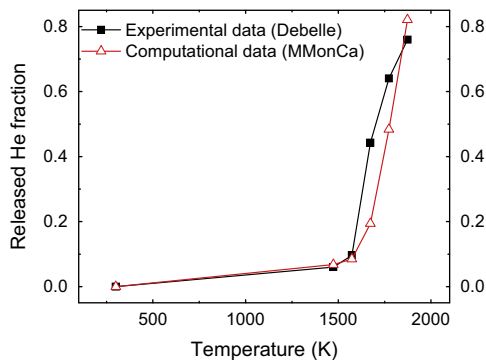

Fig. 3. Temperature evolution during and after each He pulse. During the 500 ns pulse, the temperature increases due to the incoming 625 keV He ions (red line). After the pulse, the temperature decreases until the base temperature (blue line). (For interpretation of the references to color in this figure legend, the reader is referred to the web version of this article.)

end of the implantation. Our computational results are in good agreement with the experimental ones (see Fig. 2).

2.3. Simulation of He irradiation in monocrystalline and nanocrystalline tungsten
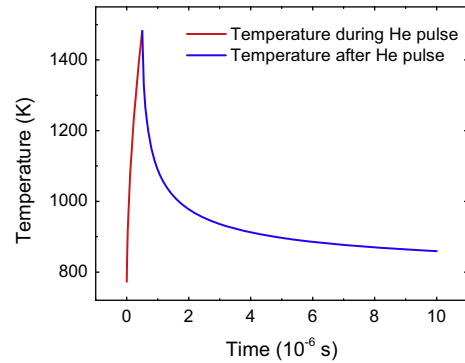
We have set a $1300 \times 50 \times 50$ nm^3 box to reproduce the pulsed irradiation conditions reported by Renk et al. [6]. They irradiated monocrystalline tungsten samples with 625 keV He ion pulses. After 400 pulses, they observed protrusions and surface pore formation in monocrystalline tungsten.

Damage cascades produced by 625 keV He ion irradiation in tungsten were simulated by the Binary Collision Approximation (BCA) code SRIM [39]. We introduce the amount of cascades corresponding to 1×10^{13} He cm^{-2} during 500 ns, that is, 2×10^{19} He cm^{-2} s^{-1} with a time step between consecutive pulses of 1 s, time enough for point defects to cluster and recombine. In order to get a more accurate simulation of the He pulses, during He implantation we take into account the temperature changes due to the energy deposition ($\sim$1 J cm^{-2}). Thus, in every pulse, the tungsten temperature increases from a base temperature of 773 K up to $\sim$1500 K followed by a fast cooling back to the base temperature in several tens of µs (Fig. 3).
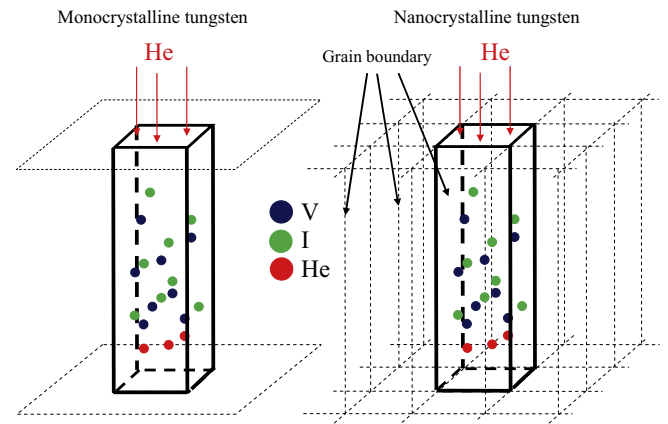
MW was simulated with periodic boundary conditions in the four lateral surfaces whereas NW was simulated assuming that the lateral surfaces act as perfect sinks (see Fig. 4). Only the defects that remain in the interior of the grains are taken into account in our results. The goal is to assess the role of grain boundaries on vacancy cluster formation and pressurization. The behavior of He
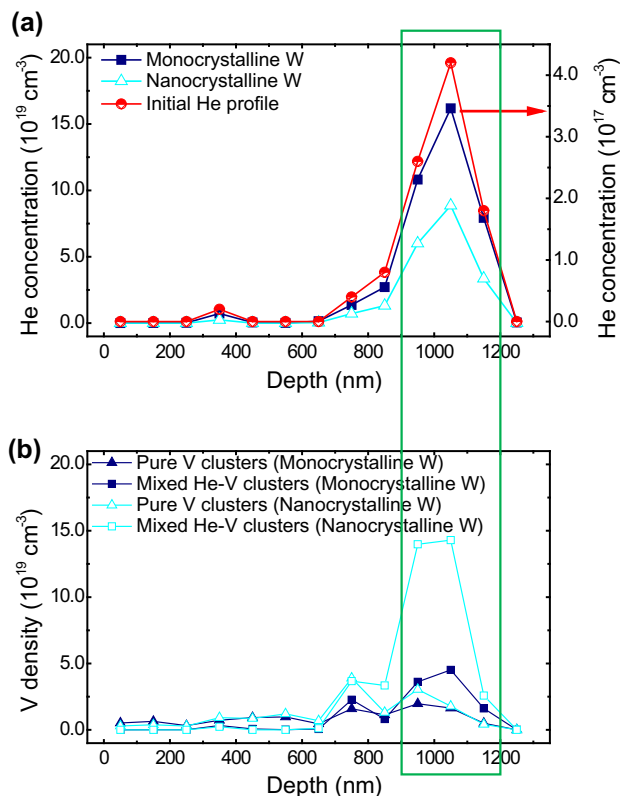

Fig. 4. Schematic view of monocrystalline and nanocrystalline tungsten simulations. In monocrystalline tungsten, periodic boundary conditions have been set in the four lateral surfaces, in order to reproduce a whole monocrystal. In nanocrystalline tungsten, the four lateral surfaces have been set as free surfaces for defects, to get the effect of grain boundaries.

and defects at grain boundaries deserves further attention since they may play an important role in the performance of W as a functional material. However, for the total fluences reached in this study we can consider that the sink character of the boundaries does not depend on the fluence. Since the grain boundary surface is very large, it is a good assumption to consider that point defects usually reached a fresh grain boundary. This justifies the fact that we consider them as perfect sinks. On the other hand, significant interstitial accumulation at the grain boundaries affects their trapping potential and requires a more sophisticated grain boundary model.

3. Results

In view of the retained He fraction, no surface He desorption is observed in our simulations. In the case of NW, an almost constant value of retained He ($\sim$50%) in the interior of the grain is reached after $\sim$100 pulses and all these He atoms are retained in He_nV_m clusters. The other 50% remains trapped at grain boundaries, assumed to be perfect sinks. In the case of MW, the He remains retained in He_nV_m clusters. The He depth profiles, Fig. 5(a) show that in both cases most He is retained in a small region between 900 and 1200 nm. We call this region the "damaged volume".

Fig. 2. Experimental (Debelle) and computational (MMonCa) data comparison in the case of He (60 keV) implantation at RT at a 2×10^{13} cm^{-2} rate and 1 h annealing at 1473 K, 1573 K, 1673 K, 1773 K and 1873 K. Experimental data published by Debelle et al. in Ref. [38].

(a)

(b)

Fig. 5. He concentration (a) and vacancy concentration as belonging to pure V clusters or to mixed He–V clusters (b) as a function of depth in monocrystalline and nanocrystalline tungsten at the end of the simulation (after 490 pulses). He profiles are compared with the He initial profile, immediately after the implantation.
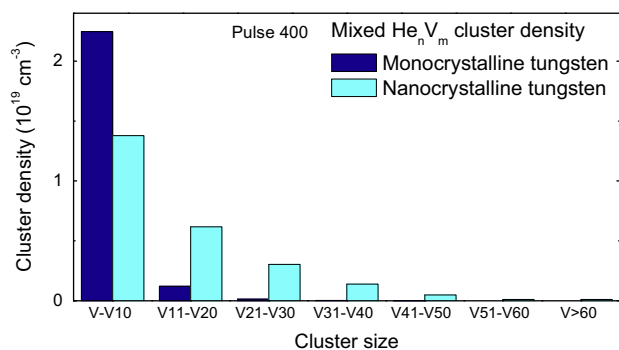
Fig. 6. Mixed He_nV_m cluster concentrations in the "damaged volume" as a function of their volume.

These profiles coincide with the as-implanted profiles obtained by SRIM, therefore, He atoms are readily retained inside mixed He_nV_m clusters near their initial position in MW and the same behavior is observed for the He atoms that remain in the interior of the grain in NW. In terms of the cluster type in which He is retained, in the case of NW all the He atoms are retained in mixed He_nV_m clusters from the very beginning of the simulation, while in the case of MW there is also a small fraction of He atoms retained in mixed He_nI_m clusters, albeit the great majority of He (more than 95%) is retained in mixed He_nV_m clusters (not shown).

Another important issue is the amount, size and distribution of vacancies. In NW there are more vacancies inside the grain than in MW Fig. 5(b). However, the difference is not very large. At the end of the simulation, the number of remaining vacancies per implanted ion is around 0.85 in MW and around 1.25 in NW. SRIM
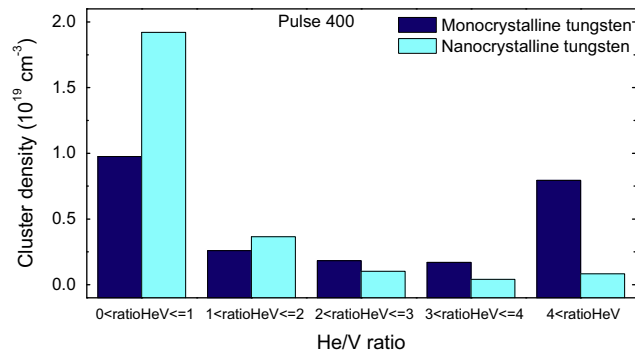
Fig. 7. Cluster density comparison between monocrystalline and nanocrystalline tungsten at the end of the simulation, as a function of the He/V ratio.

provides a value of 38.44 vacancies per ion. Thus, significant recombination $(V + I \rightarrow \varnothing)$ occurs in both cases, being slightly higher in MW. Fig. 5(b) shows the profiles of vacancies retained in the grain interior for pure vacancy (V_m) or mixed He_nV_m clusters. The vacancy profiles in pure V_m clusters are very similar in MW and NW. In both cases most of them belong to small V_m clusters with less than 10 vacancies (91% and 66%, respectively). Indeed almost all the vacancies remain isolated, i.e., they are not part of a cluster, and they distribute almost homogeneously all over the implantation volume. In the case of vacancy profiles being part of He_nV_m clusters, their distribution in depth is also similar: in both cases the mixed He_nV_m clusters are concentrated in the "damaged volume", on which we focus our attention along this study. The main difference lies in the size of the clusters. In Fig. 6 the mixed He_nV_m cluster density in the "damaged volume" is presented in histograms as a function of the number m of vacancies forming the cluster. In MW the cluster population is mainly composed of small clusters, whereas in NW significantly larger clusters are formed. That is, the grain boundaries have a direct influence on the size of mixed He_nV_m clusters.

It is crucial to know the ratio between the number of vacancies forming a cluster and the number of He atoms inside it because this parameter is related to the pressure inside the clusters. Thus, we have analyzed the He/V ratio in mixed He_nV_m clusters inside the "damaged volume". In MW, after around 200 pulses, an almost constant number of clusters of low He/V ratio is observed, whereas the density of clusters with He/V > 4 clearly increases. The results after 400 pulses show that there is almost the same density of clusters with low and high He/V ratio (see Fig. 7). On the contrary, clusters with He/V > 4 are virtually absent in NW and the great majority of clusters have a low He/V ratio.

4. Discussion

He implantation at 625 keV leads to a large amount of Frenkel Pairs (38.44 FP per implanted ion), mostly in the "damaged volume" ($300 \times 50 \times 50$ nm³) mentioned before, which is located at around 1000 nm in depth. The results show clearly that: (i) the damage is in the form of mixed He_nV_m clusters, (ii) these mixed He_nV_m clusters are concentrated in a small "damaged volume", and (iii) in the interior of a grain in NW, the He/V ratio is low and thus, low pressure is expected whereas in MW the trend is the opposite.

The diffusion of the implanted He atoms is in competition with more effective trapping at vacancy-type defects, resulting in a negligible diffusion out of the "damaged volume" and the formation of immobile mixed He_nV_m clusters. He dissociation energies from these defects are high (Table 3) suppressing He release at moderate

temperatures (those employed in this study) and resulting in 100% He retention in MW. This behavior was pointed out by Debelle et al. in Ref. [40] in the case of He irradiation at 500 keV. They implanted [3]He (500 keV) in polycrystalline tungsten at three different fluences (10^{15}, 10^{16}, and 5×10^{16} cm^{-2}) followed by a thermal annealing at 1473 K (during 70 min) or at 1773 K (during 60 min). Contrary to He desorption observed in their experiments of He irradiation at 60 keV [38], in the case of He irradiation at 500 eV they observed no He desorption, with a relative precision of ∼3%. Gilliam et al. [41] also implanted [3]He in similar conditions (1.3 MeV up to 5×10^{16} cm^{-2}) and they did neither observe any change in He retention after flash annealings at 2273 K. Our simulations (MW) are in good agreement with these experimental results. In the case of NW the process is similar. No desorption from the free surface occurs and there is also 100% He retention. However, the close vicinity to grain boundaries (grain dimensions $1300 \times 50 \times 50$ nm^3), assumed as perfect sinks, leads to effective immobilization of He atoms (50%) inside them. To evaluate the influence of grain size and therefore, the grain boundary density, we have also simulated 625 keV He irradiation in nanocrystalline tungsten with larger grains, i.e., lower grain density (grain dimensions $1300 \times 100 \times 100$ nm^3). The results (not shown) reveal a clear trend: the lower the grain boundary density, the higher the He retention in He$_n$V$_m$ clusters formed in the grain interior (20% higher compared with $1300 \times 50 \times 50$ nm^3 grains), which evidences a clear relationship between grain boundary density and the amount of He retained in He$_n$V$_m$ clusters.

In the present simulations, tungsten temperature reaches ∼1500 K just after the He pulse and then drops very rapidly (Fig. 3). Most of the time the temperature is 773 K (base temperature). Although migration energy of single vacancy is high (Table 1), this temperature is high enough to promote some vacancy movement. However, they turn out to be not very mobile and remain near their initial positions. Neither in MW nor in NW can vacancies reach the free surface. In NW only a small fraction of them reaches the surrounding grain boundaries. The higher amount of vacancies in NW comparing to MW is determined by defect annihilation (V + I → ∅), not by vacancy mobility. SIAs migrate so fast at the simulation temperatures (Table 1) that they can reach the free surface in the case of MW and not only the free surface but also the surrounding grain boundaries in the case of NW. In the latter case, these SIAs bind to the grain boundary before finding a vacancy to annihilate with, leading to a larger amount of vacancies in the interior of the grain.

There is almost no He retained in mixed He$_n$I$_m$. We can explain this behavior as follows: on the one hand, the binding energies of He atoms to mixed He$_n$I$_m$ clusters [32] are lower than the binding energies to mixed He$_n$V$_m$ and thus, more efficient emission from He$_n$I$_m$ clusters occurs. On the other hand, the vacancy mobility is much lower than the SIA mobility (see Table 1), which results in a much larger vacancy population than SIA population inside tungsten. Thus, the great majority of He atoms are trapped at vacancy clusters. A similar behavior is described in the simulations carried out by De Backer et al. [42], in the case of tungsten implanted at room temperature with 800 keV [3]He atoms and subsequently annealed from 300 K to 900 K, at fluences from 10^{17} to 5×10^{16} ions cm^{-2}.

As a result, in both MW and NW almost all the He atoms are retained in mixed He$_n$V$_m$ clusters in the "damaged volume". A better understanding of the size and composition of these mixed He$_n$V$_m$ clusters will lead to a better understanding of the whole problem, as they control the response of the material to He irradiation.

Fig. 7 shows the cluster density as a function of their He/V ratio in both MW and NW after 400 pulses. In NW, we can see that the majority of the clusters have a low He/V ratio. After the formation
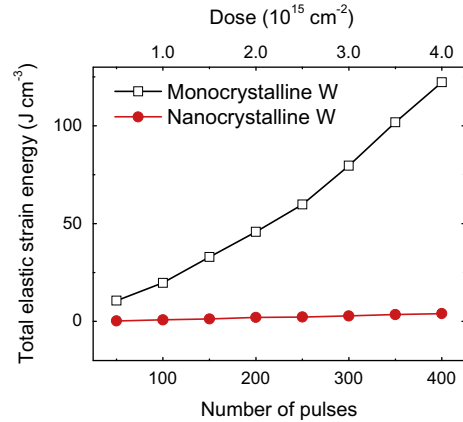

Fig. 8. Total elastic strain energy as a function of the number of pulses. We have calculated the elastic strain energy corresponding to each He$_n$V$_m$ cluster [43]. The figure represents the sum of all of them in both monocrystalline and nanocrystalline tungsten.

of a certain amount of immobile mixed He$_n$V$_m$ clusters, the incoming He ions from later pulses are mainly retained inside them. As there are more vacancies per implanted He ion after each pulse (1.25 remaining vacancies per implanted ion), these clusters tend to maintain the He/V ratio or even decrease its value. Thus, we do not expect a significant increase of the pressure inside the grains in NW with the increasing number of pulses. In MW there are 0.85 remaining vacancies per implanted He. The He/V ratio tends to increase with the increasing number of pulses, leading to a lower cluster density with lower He/V ratio and a higher density of clusters with He/V ratio > 4. This indicates that pressure seriously increases with the number of pulses.

The different defect configuration in MW and in NW may lead to a different mechanical behavior, since the size and He/V ratio of mixed He$_n$V$_m$ clusters have an influence on it. We have compared the total elastic strain energy in both cases, calculated as the sum of the elastic strain energy generated by each single cluster making use of the equation published by Wolfer [43]. This equation takes into account not only the pressure inside each He$_n$V$_m$ cluster (p_i) but also its volume (V_0):

$$E_p(p_i) = \frac{3V_0 p_i^2}{8\mu} \tag{4}$$

where E_p is the elastic strain energy and μ the shear modulus of tungsten. We have assumed that the volume of the mixed He$_n$V$_m$ clusters is the sum of the volume of each vacancy: $V_0 = m \cdot V_1$, where V_1 is the volume of a single vacancy: $V_1 = 4/3 \cdot \pi \cdot (a/2)^3$ and a is the lattice parameter of tungsten (a = 3.172 Å). In order to calculate the pressure inside these mixed He$_n$V$_m$ clusters, we have used the Mills-Liebenberg-Bronson (MLB) semiempirical equation of state (EOS) [44]. Although the limits of MLB-EOS are 0.2 < P < 2 GPa [44], Donnelly [14] used this EOS even at a pressure 50 times higher than the upper limit (up to 100 GPa) and it is widely used nowadays [36,45] for this purpose. The evolution of the total elastic strain energy in MW and inside a grain in NW as a function of the number of pulses is shown in Fig. 8. The trend is clear: in MW, the elastic strain energy increases while in the interior of a grain in NW the increase of the elastic strain energy is negligible, as it remains almost constant. Although at the beginning of the irradiation the difference between both materials is not so high, after 400 pulses the elastic strain energy in MW is 122.24 J cm^{-3} and in the interior of a grain in NW it takes a value of 4.03 J cm^{-3}. This result shows that the interior of a grain in NW will be subjected to a lower stress than the MW, extending the life service of the material.

Gao et al. [46,47] suggest for iron at room temperature that these overpressurized He_nV_m clusters will deform the lattice around them and finally the emission of a SIA will occur to release the pressure inside. This emitted SIA is bound to the He_nV_m cluster and remains in its surroundings, as was observed experimentally in steel [48]. This leads to more defects present inside the lattice. Similar mechanisms are proposed for He in tungsten [34,35,49] but they are not included in our simulations: although these mechanisms are available in MMonCa, a good parameterization for them is necessary. These mechanisms are called "trap mutation" and "self trapping". The "trap mutation" mechanism consists in the emission of an interstitial due to a high pressurized He_nV_m cluster ($He_nV_m \rightarrow He_nV_{m+1} + I$) and the "self trapping" is a similar process, but the emission of an interstitial is due to a pure He cluster ($He_n \rightarrow He_nV + I$), which will remain inside the created vacancy. These mechanisms are crucial in the case of He irradiation at very high fluence ($\sim 10^{20}$ He cm^{-2}) and low energy (~ 300 eV). He ions at such a low energy do not produce Frenkel Pairs in tungsten and all the vacancies are created by these mechanisms. On the contrary we simulate He irradiation at 625 keV, high enough to produce a large amount of Frenkel Pairs. The number of clusters with very high He/V ratio (He/V ~ 9) is negligible and the formation of large pure He clusters is also insignificant. Thus, neither "trap mutation" nor "self trapping" are expected to be relevant in our simulations.

5. Conclusions

We have used an OKMC model parameterized with DFT data to simulate He irradiation in tungsten up to a fluence of $\sim 10^{16}$ ion cm^{-2} and a relatively high temperature (up to 1500 K). A comparison with experimental data on He desorption has been carried out in order to validate our parameterization at these temperatures. Our results are in good agreement with the experimental ones.

Simulations of 625 keV He ion irradiation in MW and NW reveal 100% He retention and the appearance of different defect configurations. In NW, around 50% of the incoming He ions are retained at the grain boundaries and the other 50% in the interior of a grain of dimensions $1300 \times 50 \times 50$ nm^3. In the case of larger grains, the amount of He retention at the grain boundaries decreases: in a grain four times larger, of dimensions $1300 \times 100 \times 100$ nm^3, this value drops down to $\sim 30\%$, revealing a high dependence of grain boundary density on the mechanisms of He retention.

The amount and distribution of pure vacancy clusters (V_m) are similar in both cases. Mixed He_nV_m clusters turn to be concentrated in a small "damaged volume" at around 1000 nm. On the other hand, the size and number of He atoms inside the mixed He_nV_m clusters is different in the interior of a grain in NW and in MW. The trend is clear: in NW, mixed He_nV_m clusters are larger (they have more vacancies) and their He/V ratio is lower. Therefore, mixed He_nV_m clusters are less pressurized in the interior of a grain in NW.

The value of the elastic strain energy is lower in the interior of the grain in NW than in MW. Moreover, while in MW a significant increase in the elastic strain energy is observed, in NW it remains almost constant. We can conclude that NW would be able to resist the deleterious effects of irradiation better than MW. In addition to this, if the trend observed in these results remains the same with the increasing number of pulses, a much better response of NW will then be expected at higher He irradiation fluence.

Acknowledgements

References

[1] J.W. Davis, V.R. Barabash, A. Makhankov, L. Plöchl, K.T. Slattery, J. Nucl. Mater 258–263 (Part 1) (1998) 308.
[2] R.E. Nygren, D.L. Youchison, R.D. Watson, S. O'Dell, Fusion Eng. Des. 49–50 (2000) 303.
[3] J.D. Sethian, A.R. Raffray, J. Latkowski, J.P. Blanchard, L. Snead, T.J. Renk, S. Sharafat, J. Nucl. Mater. 347 (2005) 161.
[4] J.D. Sethian, D.G. Colombant, J.L. Giuliani, R.H. Lehmberg, M.C. Myers, S.P. Obenschain, A.J. Schmitt, J. Weaver, M.F. Wolford, F. Hegeler, M. Friedman, A.E. Robson, A. Bayramian, J. Caird, C. Ebbers, J. Latkowski, W. Hogan, W.R. Meier, L.J. Perkins, K. Schaffers, S. Abdel Kahlik, K. Schoonover, D. Sadowski, K. Boehm, L. Carlson, J. Pulsifer, F. Najmabadi, A.R. Raffray, M.S. Tillack, G. Kulcinski, J.P. Blanchard, T. Heltemes, A. Ibrahim, E. Marriott, G. Moses, R. Radell, M. Sawan, J. Santarius, G. Sviatoslavsky, S. Zenobia, N.M. Ghoniem, S. Sharafat, J. El-Awady, Q. Hu, C. Duty, K. Leonard, G. Romanoski, L.L. Snead, S.J. Zinkle, C. Gentile, W. Parsells, C. Prinksi, T. Kozub, T. Dodson, D.V. Rose, T. Renk, C. Olson, N. Alexander, A. Bozek, G. Flint, D.T. Goodin, J. Hund, R. Paguio, R.W. Petzoldt, D.G. Schroen, J. Sheliak, T. Bernat, D. Bittner, J. Karnes, N. Petta, J. Streit, D. Geller, J.K. Hoffer, M.W. McGeoch, S.C. Glidden, H. Sanders, D. Weidenheimer, D. Morton, I.D. Smith, M. Bobecia, D. Harding, T. Lehecka, S.B. Gilliam, S.M. Gidcumb, D. Forsythe, N.R. Parikh, S. O'Dell, M. Gorensek, IEEE Trans. Plasma Sci. 38 (2010) 690.
[5] G. Federici, P. Andrew, P. Barabaschi, J. Brooks, R. Doerner, A. Geier, A. Herrmann, G. Janeschitz, K. Krieger, A. Kukushkin, A. Loarte, R. Neu, G. Saibene, M. Shimada, G. Strohmayer, M. Sugihara, J. Nucl. Mater. 313–316 (2003) 11.
[6] T.J. Renk, P.P. Provencio, T.J. Tanaka, J.P. Blanchard, C.J. Martin, T.R. Knowles, Fusion Sci. Technol. 61 (2012) 57.
[7] J. Alvarez Ruiz, A. Rivera de Mena, R. Gonzalez Arrabal, D. Garoz Gómez, E. del Rio Redondo, J.M. Perlado Martin, Fusion Sci. Technol. 60 (2011) 565.
[8] A.R. Raffray, J. Nucl. Mater. 347 (2005) 178.
[9] A.R. Raffray, J. Blanchard, J. Latkowski, F. Najmabadi, T. Renk, J. Sethian, S. Sharafat, L. Snead, Fusion Eng. Des. 81 (2006) 1627.
[10] J.P. Blanchard, C.J. Martin, J. Nucl. Mater. 347 (2005) 192.
[11] J. Alvarez, R. Gonzalez-Arrabal, A. Rivera, E. Del Rio, D. Garoz, E.R. Hodgson, F. Tabares, R. Vila, M. Perlado, Fusion Eng. Des. 86 (2011) 1762.
[12] A.R. Raffray, L. El-Guebaly, G. Federici, D. Haynes, F. Najmabadi, D. Petti, Fusion Sci. Technol. 46 (2004) 417.
[13] H. Trinkaus, Radiat. Eff. 78 (1983) 189.
[14] S.E. Donnelly, Radiat. Eff. 90 (1985) 1.
[15] S. Sharafat, A. Takahashi, Q. Hu, N.M. Ghoniem, J. Nucl. Mater. 386–388 (2009) 900.
[16] S. Kajita, W. Sakaguchi, N. Ohno, N. Yoshida, T. Saeki, Nucl. Fusion 49 (2009) 095005.
[17] S.J. Zenobia, G.L. Kulcinski, Phys. Scr. 2009 (2009) 014049.
[18] S.J. Zenobia, L.M. Garrison, G.L. Kulcinski, J. Nucl. Mater. 425 (2012) 83.
[19] V.N. Chernikov, A.P. Zakharov, J. Nucl. Mater. 165 (1989) 89.
[20] G.J. Thomas, Radiat. Eff. 78 (1983) 37.
[21] H. Iwakiri, K. Yasunaga, K. Morishita, N. Yoshida, J. Nucl. Mater 283–287 (Part 2) (2000) 1134.
[22] N. Gordillo, M. Panizo-Laiz, E. Tejado, I. Fernandez-Martinez, A. Rivera, J.Y. Pastor, C.G. de Castro, J. del Rio, J.M. Perlado, R. Gonzalez-Arrabal, Appl. Surf. Sci. 316 (2014) 1.
[23] R. Gonzalez-Arrabal, M. Panizo-Laiz, N. Gordillo, E. Tejado, F. Munnik, A. Rivera, J.M. Perlado, J. Nucl. Mater. 453 (2014) 287.
[24] I. Martin-Bragado, A. Rivera, G. Valles, J.L. Gomez-Selles, M.J. Caturla, Comput. Phys. Commun. 184 (2013) 2703.
[25] <http://materials.imdea.org/MMonCa>..
[26] G. Kresse, D. Joubert, Phys. Rev. B 59 (1999) 1758.
[27] G. Kresse, J. Furthmuller, Phys. Rev. B 54 (1996) 11169.
[28] G. Kresse, J. Hafner, Phys. Rev. B 47 (1993) 558.
[29] J.P. Perdew, K. Burke, M. Ernzerhof, Phys. Rev. Lett. 77 (1996) 3865.
[30] P. Blochl, Phys. Rev. B 50 (1994) 17953.
[31] C.S. Becquart, C. Domain, J. Nucl. Mater. 385 (2009) 223.
[32] C.S. Becquart, C. Domain, U. Sarkar, A. DeBacker, M. Hou, J. Nucl. Mater. 403 (2010) 75.
[33] C. González, R. Iglesias, J. Mater. Sci. 49 (2014) 8127.
[34] A. Takayama, A.M. Ito, S. Saito, N. Ohno, H. Nakamura, Jpn. J. Appl. Phys 52 (2013). 01AL03.
[35] T. Tamura, R. Kobayashi, S. Ogata, A.M. Ito, Model. Simul. Mater. Sci. Eng. 22 (2014) 015002.
[36] K.O.E. Henriksson, K. Nordlund, J. Keinonen, Nucl. Instrum. Methods Phys. Res. Sect. B Beam Interact. Mater. At 244 (2006) 377.

[37] N. Juslin, B.D. Wirth, J. Nucl. Mater. 432 (2013) 61.
[38] A. Debelle, P.-E. Lhuillier, M.-F. Barthe, T. Sauvage, P. Desgardin, Nucl. Instrum. Methods Phys. Res. Sect. B Beam Interact. Mater. At 268 (2010) 223.
[39] <http://www.srim.org/>..
[40] A. Debelle, M.F. Barthe, T. Sauvage, R. Belamhawal, A. Chelgoum, P. Desgardin, H. Labrim, J. Nucl. Mater. 362 (2007) 181.
[41] S.B. Gilliam, S.M. Gidcumb, N.R. Parikh, D.G. Forsythe, B.K. Patnaik, J.D. Hunn, L.L. Snead, G.P. Lamaze, J. Nucl. Mater. 347 (2005) 289.
[42] A. De Backer, P.E. Lhuillier, C.S. Becquart, M.F. Barthe, J. Nucl. Mater. 429 (2012) 78.
[43] W. Wolfer, Philos. Mag. -Phys. Condens. Matter Struct. Defects Mech. Prop. 58 (1988) 285.
[44] R.L. Mills, D.H. Liebenberg, J.C. Bronson, Phys. Rev. B 21 (1980) 5137.
[45] N. Li, M. Nastasi, A. Misra, Int. J. Plast. 32–33 (2012) 1.
[46] N. Gao, H.V. Swygenhoven, M. Victoria, J. Chen, J. Phys. Condens. Matter 23 (2011) 442201.
[47] N. Gao, M. Victoria, J. Chen, H. Van Swygenhoven, J. Phys. Condens. Matter Inst. Phys. J. 23 (2011) 245403.
[48] J. Chen, P. Jung, W. Hoffelner, H. Ullmaier, Acta Mater. 56 (2008) 250.
[49] J. Boisse, C. Domain, C.S. Becquart, J. Nucl. Mater. 455 (2014) 10.